JACC: BASIC TO TRANSLATIONAL SCIENCE VOL. 5, NO. 5, 2020

PRECLINICAL RESEARCH

Changes in Myocardial Microstructure and Mechanics With Progressive Left Ventricular Pressure Overload

William M. Torres, PhD,[a,b] Shayne C. Barlow, DVM, PhD,[b] Amber Moore, BS,[b] Lisa A. Freeburg, BS,[b] Abigail Hoenes, BS,[b] Heather Doviak, BS,[b] Michael R. Zile, MD,[c] Tarek Shazly, PhD,[a] Francis G. Spinale, MD, PhD[a,b]

VISUAL ABSTRACT

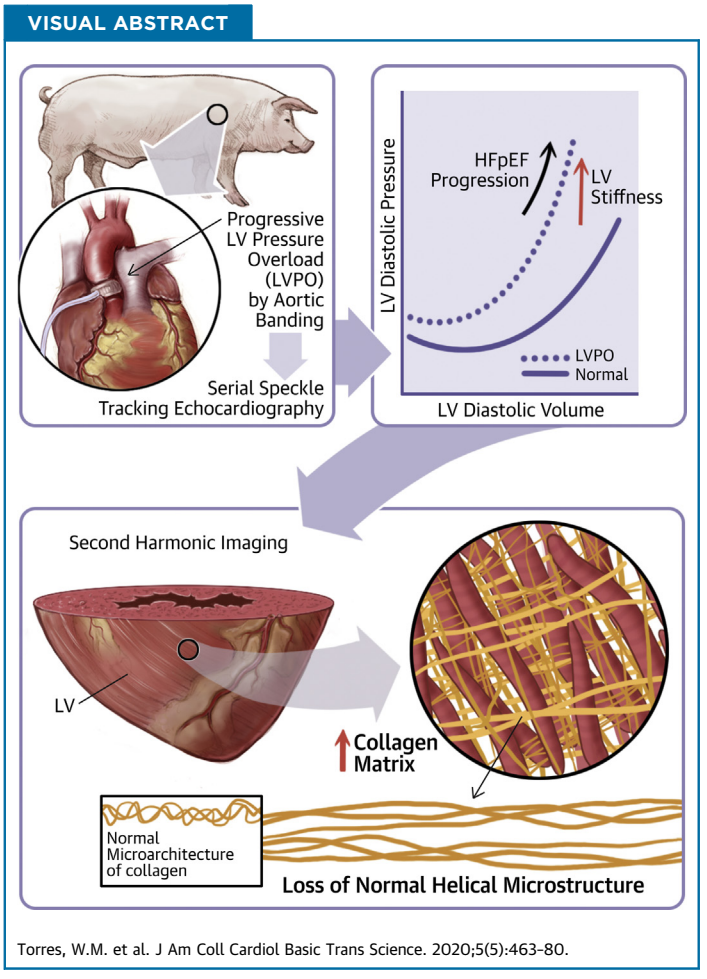

Torres, W.M. et al. J Am Coll Cardiol Basic Trans Science. 2020;5(5):463–80.

HIGHLIGHTS

- **A large animal model of progressive PO was created that evolved into phenotypic features of HFpEF.**
- **The progression from PO to the HFpEF pathophysiology was accompanied by specific shifts in the collagen matrix microstructure over and above collagen content (i.e., fibrosis).**
- **Using early changes in regional myocardial stiffness measurements by speckle tracking methodology predicted the extent and magnitude of the HFpEF phenotype at later timepoints.**

ISSN 2452-302X https://doi.org/10.1016/j.jacbts.2020.02.007

JACC: BASIC TO TRANSLATIONAL SCIENCE VOL. 5, NO. 5, 2020
MAY 2020:463–80

ABBREVIATIONS AND ACRONYMS

Ct = cycle time

EDV = end-diastolic volume

EF = ejection fraction

ESV = end-systolic volume

HF = heart failure

HFpEF = heart failure with preserved ejection fraction

HFrEF = heart failure with reduced ejection fraction

IVRT = isovolumic relaxation time

LA = left atrial

LV = left ventricular

LVPO = left ventricular pressure overload

NT-proBNP = N-terminal pro-brain natriuretic peptide

PCR = polymerase chain reaction

PRSW = pre-load recruitable stroke work

qPCR = quantitative real-time PCR

SHG = second harmonic generation

STE = speckle tracking echocardiography

SUMMARY

This study assessed the regional changes in myocardial geometry, microstructure, mechanical behavior, and properties that occur in response to progressive left ventricular pressure overload (LVPO) in a large animal model. Using an index of local biomechanical function at early onset of LVPO allowed for prediction of the magnitude of left ventricular chamber stiffness (Kc) and left atrial area at LVPO late timepoints. Our study found that LV myocardial collagen content alone was insufficient to identify mechanisms for LV myocardial stiffness with progression to heart failure with preserved ejection fraction (HFpEF). Serial assessment of regional biomechanical function might hold value in monitoring the natural history and progression of HFpEF, which would allow evaluation of novel therapeutic approaches. (J Am Coll Cardiol Basic Trans Science 2020;5:463–80)

The rate and incidence of heart failure (HF) continues to escalate, and recent statistics have identified this disease as the leading cause of morbidity and mortality—eclipsing all other chronic diseases (1). Although significant progress has been achieved in therapeutic retardation or elimination of other major illnesses (e.g., such as cancer), these advancements have not been as forthcoming for HF. One contributory factor for this is that, unlike cancer, which is classified by morphology, cell type, and molecular and/or genetic profiles, HF has been historically considered to be a single entity fundamentally defined by symptomatology. However, it must be recognized that HF arises from distinctly different etiologies, which, in turn, have demonstrated distinctly different therapeutic responses and clinical outcomes (2,3). Although the precise categorization of HF is continuously evolving, a generalized dichotomy can be made between patients with HF who present with or without significant left ventricular (LV) pump dysfunction. Specifically, if LV ejection fraction (EF) is impaired, this is defined as HF with reduced EF (HFrEF), whereas if HF symptoms are present and EF is within normal limits, then the definition of HF with a preserved EF (HFpEF) is used. It has been estimated that patients with these HF phenotypes are equally distributed (2). Randomized clinical trials using combinatorial pharmacology or device-driven therapies have demonstrated significant improvement in clinical outcomes in patients with HFrEF but not in patients with HFpEF (4–11). In addition, although the functional progression of HFrEF can be monitored by serial assessment of changes in EF, the natural history of HFpEF is not as easily assessed or well-understood (12,13).

One-rate limiting step in the research progress for HFpEF is a paucity of translationally relevant animal models that recapitulate key phenotypical features of the clinical syndrome of HFpEF (14,15). Specifically, HFpEF can arise from progressive and prolonged LV pressure overload (LVPO) rather than from an acute pathological stimulus (e.g., myocardial ischemia) that progresses to HFrEF (16–19). In addition, a key component in the progression of HFpEF is the development of LV diastolic dysfunction, for which detection requires sensitive measures of LV diastolic performance that can be difficult to assess in a serial manner (20,21).

We used a previously established porcine model of progressive LVPO that resulted in significant LV

From the [a]College of Engineering and Computing, University of South Carolina, Columbia, South Carolina; [b]Cardiovascular Translational Research Center, University of South Carolina School of Medicine and the Columbia Veteran Affairs Healthcare Center, Columbia, South Carolina; and the [c]Medical University of South Carolina and RHJ Department of Veterans Affairs Medical Center, Charleston, South Carolina. This work was supported by the National, Heart, Lung, and Blood Institute of the National Institutes of Health (R01HL130972 and 3R01HL130972-01A1S1). The content is solely the responsibility of the authors and does not necessarily represent the official views of the National Institutes of Health. The authors have reported that they have no relationships relevant to the contents of this paper to disclose.

The authors attest they are in compliance with human studies committees and animal welfare regulations of the authors' institutions and Food and Drug Administration guidelines, including patient consent where appropriate. For more information, visit the *JACC: Basic to Translational Science* author instructions page.

Manuscript received June 10, 2019; revised manuscript received February 27, 2020, accepted February 28, 2020.

hypertrophy with stable EF but with evidence for impaired diastolic function that was consistent with the clinical phenotype of HFpEF (22). The central hypothesis of this study was that LV myocardial remodeling in response to progressive LVPO is characterized by an increase in LV myocardial collagen content and a change in collagen fiber microstructure, which together will affect both regional LV myocardial mechanical properties and LV chamber stiffness. To test this hypothesis, we developed and deployed novel and innovative approaches based on noninvasive imaging to assess LV regional diastolic function together with advanced optical analysis of LV myocardial collagen microstructure. We used obtained data to build a mechanics-based mathematical model that predicts the rate and magnitude of LV chamber stiffness elevations with progressive LVPO. Our findings supported the continued consideration of progressive LVPO as a preclinical model for the clinical syndrome of HFpEF and demonstrated the potential clinical value of assessing regional LV myocardial biomechanical function to monitor HFpEF progression.

METHODS

Progressive LVPO was induced in pigs for up to a 5-week period, during which regional LV myocardial strain and stiffness were quantified using speckle tracking echocardiography (STE). At terminal timepoints, LV myocardial collagen content was quantified using quantitative histomorphometry, LV myocardial microstructure was assessed using second harmonic generation (SHG) imaging, and select biochemical markers were quantified using immunohistochemistry and targeted gene analysis (23–29). LV myocardial functional response variables were assessed in a serial fashion focusing on identifying factors that would contribute to and potentially predict changes in LV chamber stiffness, a hallmark of HFpEF progression (22,30–37).

LVPO INDUCTION. Yorkshire pigs (n = 14; 15.8 ± 0.6 kg; Hambone Farms, Orangeburg, South Carolina) were anesthetized with isoflurane (3%/1.5 l/min), and through a left thoracotomy, a 12-mm inflatable silastic vascular cuff (Access Technologies, Skokie, Illinois) was secured around the supracoronary ascending aorta without inducing aortic constriction. A length of silastic tubing was connected to a subcutaneous access port (Access Technologies) for subsequent hydraulic expansion of the aortic cuff. After a 1-week recovery period, the cuff was inflated through the access port (via 0.45 ml glycerol) to achieve a specific target gradient of 75 mm Hg across the cuff and thus induce LVPO. At weekly intervals thereafter, the cuff was further inflated (0.25-ml increments) to cause a stepwise increase in the pressure gradient (25 mm Hg increase and/or inflation). At either 4 weeks (n = 7) or 5 weeks (n = 7) post-LVPO, the animals were anesthetized (5% isoflurane), and the LV was harvested. Age-matched referent control pigs (n = 12) were used for comparative analyses. All animals were treated and cared for in accordance with the National Institutes of Health Guide for the Care and Use of Laboratory Animals (Eighth Edition; Washington, DC: 2011), and all experimental protocols were approved by Institutional Animal Care and Use Committees at the University of South Carolina.

SERIAL LV ECHOCARDIOGRAPHY. LV echocardiography was performed weekly throughout the study (GE Vivid E9 with XDclear Ultrasound System: M5S [1.5 to 4.6 MHz] transducer probe; GE, Boston, Massachusetts). LV and left atrial (LA) dimensions and function were assessed by 2-dimensional and M-mode echocardiographic studies, as described previously (38,39). From the obtained LV measurements, LV end-diastolic volume (EDV), end-systolic volume (ESV), and EF were calculated using the biplane method of disks. LA area was determined from the anteroposterior dimensions acquired from the parasternal long-axis view. LV wall thickness was determined and LV mass computed using conventional formulas (40). Finally, LV isovolumic relaxation time (IVRT) was measured by tissue Doppler imaging M-mode through the mitral leaflet (41).

DEFINITION OF NORMAL RANGE FOR LV MASS. LV mass measurements and body weights were examined from an archived data set of control pigs (100 pigs; body weight: 13 to 33 kg). These data allowed for the construction of a normogram for LV mass as a function of body weight (linear regression and a 95% confidence interval) and thus provided a basis to assess LVPO-mediated changes in LV mass with respect to normal growth.

STE. Three consecutive digital loops of the 2-dimensional echocardiography for the LV long and short-axes were stored on a hard disk and transferred to a workstation (EchoPac, Vingmed, General Electric) for post-processing. For each echocardiographic digital loop, a region of interest was defined at the onset of the R-wave and then discretized with a spatial mesh of acoustic clusters on a frame-to-frame basis throughout the cardiac cycle (R-R interval) (26). Following grouping of the acoustic clusters into 6

predetermined anatomical regions, tracking of the region of interest allowed for the definition of segmental lengths at end-diastole ($L0$) and continuously throughout the cardiac cycle (L). Regional LV myocardial segmental strains (ε) and strain rates (γ) were then computed as:

$$\varepsilon = \frac{L - L_0}{L_0} = \frac{\Delta L}{L_0} \quad \text{(Eq. 1)}$$

$$\gamma = \frac{(\Delta L/\Delta t)}{L_0} \quad \text{(Eq. 2)}$$

where Δt is the relative time in the cardiac cycle. LV myocardial peak strains and diastolic strain rates were quantified in 2 normal directions, circumferential (short axis) and longitudinal (long axis), at the endocardial, mid-wall, and epicardial surfaces. Global LV myocardial strain values were calculated based on the total length change of all 6 segments. Obtained LV myocardial segmental strain and strain rate data were assessed for intraobserver variance by calculating the intraclass correlation coefficient for a single operator under the assumption that systematic differences were relevant. The intraclass correlation coefficient for all measures of LV myocardial strain and strain rate ranged from 0.94 to 0.99.

REGIONAL LV MYOCARDIAL WALL STRESS. We modified a thick-walled ellipsoidal model proposed by Janz (42) to compute regional LV myocardial wall stress in the circumferential and longitudinal directions. The regional circumferential LV myocardial wall stress (σ_C) was computed as:

$$\sigma_C = \frac{Pr^2}{2t\left(r + \frac{t}{2}\right)} \quad \text{(Eq. 3)}$$

where r is the inner radius, t is the regional wall thickness, and P is LV pressure. For the purposes of this study, LV pressure was assumed to equal zero at the onset of diastole. An estimated value at end-diastole (described in the following) regional longitudinal LV myocardial wall stress (σ_L) was computed as:

$$\sigma_L = \frac{Pr^2}{2t(\sin\Phi)\left(r + \frac{t(\sin\Phi)}{2}\right)} \quad \text{(Eq. 4)}$$

where Φ is the angle between the normal vector from the endocardium at the region of interest and the axis of revolution in the truncated ellipsoid model.

REGIONAL LV DIASTOLIC MYOCARDIAL STIFFNESS. Obtained values for regional LV myocardial wall stress and segmental myocardial strain at the onset of diastole and at end-diastole enabled calculation of regional LV diastolic myocardial stiffness in both the circumferential and longitudinal directions. The slope of the line between these 2 points in the stress-strain plane, developed in the defined anatomical regions, was used to compute the regional LV diastolic myocardial stiffness (κ_{MR}) as:

$$\kappa_{MR} = \frac{\sigma_{ED}}{|\varepsilon_{D0}|} \quad \text{(Eq. 5)}$$

where σ_{ED} and ε_{D0} are the regional end-diastolic LV myocardial wall stress and LV segmental myocardial strain at the onset of diastole, respectively (39).

NONINVASIVE ESTIMATION OF LV END-DIASTOLIC PRESSURE AND LV CHAMBER STIFFNESS. To facilitate serial biomechanical analyses of the LV, we developed a noninvasive estimation of LV end-diastolic pressure (P_{ED}) via relation of the LA area to invasively measured pulmonary capillary wedge pressure. Briefly, a cohort of referent control (n = 5) and LVPO (n = 8) pigs were anesthetized (fentanyl 50 and propofol 100 mg), and a multilumened thermodilution catheter (7.5F, Baxter Healthcare Corp., Irvine, California) was then advanced through the right external jugular vein and positioned in the pulmonary artery. Pulmonary capillary wedge pressure, a surrogate for P_{ED}, was measured using conventional methods (43). Data were used to identify an expression for noninvasive estimation of LV end-diastolic pressure, specifically $P_{ED} = 1.88e^{0.16(\text{LA area})}$ ($r^2 = 0.91$), which was subsequently applied across the study groups. This pressure estimation was used to compute a noninvasive measure of LV chamber stiffness (K_C^*) as follows (39):

$$K_C^* = \frac{P_{ED}}{EDV} \quad \text{(Eq. 6)}$$

INVASIVE MEASURES OF LV PRESSURE AND LV CHAMBER STIFFNESS. To validate noninvasive biomechanical measures, invasive LV pressure and dimensions were obtained in a subset of referent control (n = 6) 4 weeks post-LVPO (n = 4), and 5 weeks post-LVPO (n = 4) pigs. A pre-calibrated microtipped transducer (7.5F, Millar Instruments Inc., Houston, Texas) was placed in the LV through a small apical stab wound. LV pressure data were recorded at a sampling frequency of 100 Hz and digitized (Ponemah, Harvard Bioscience Inc., Hollis-ton, Massachusetts). Following the placement of instrumentation, an ultrasound transducer (GE Vivid E9 with XDclear Ultrasound System: M5S [1.5 to 4.6 MHz] transducer probe) was positioned for

transthoracic imaging of the LV short axis and measurement of continuous LV volume and wall thickness (44). Steady-state LV function was determined with simultaneous acquisition of LV pressure and echocardiographic data, with the ventilator temporarily suspended to prevent respiratory artifact. After steady-state measurements, LV pre-load was altered with sequential occlusion and release of the inferior vena cava with vascular ligature. Again, simultaneous LV pressure and echocardiographic data were collected during occlusion and release.

After data acquisition was complete, the digitized LV pressure and dimension data were aligned using the R-wave of the simultaneously recorded electrocardiogram from each modality. The aligned data for the steady-state and caval occlusion cardiac cycles were then used to compute the regional LV myocardial stiffness constants (κ_{MR}) and LV chamber stiffness (K_C), respectively (45,46). In addition, data were processed to compute classic indexes of LV systolic function and LV diastolic function using established methods (47–49).

SHG IMAGING. LV myocardial collagen microstructure was analyzed in subset of the referent control (n = 5), 4 weeks post-LVPO (n = 6), and 5 weeks post-LVPO (n = 7) pigs using SHG imaging. Briefly, the pigs were euthanized (5% isoflurane), the LV removed, and a 1-inch thick circumferential section was fixed in 10% formalin—preserving the native orientation and configuration of the LV myocardial collagen fibers—for 24 h at 4°C. The LV lateral free-wall myocardium was later sectioned into 200 μm sections and placed on the motorized stage of a multiphoton microscope (Leica TCS SP8 MP, Leica Microsystems). Short-pulsed infrared lasers were used to create nonlinear polarization effects in the form of SHG signals at a magnification of 25×. SHG images were acquired for a fixed sample area of 0.2 mm^2 at depth intervals of 1.5 μm.

AUTOMATED TRACING OF INDIVIDUAL COLLAGEN FIBERS. Two-dimensional images acquired from the multiphoton microscope were converted to 8-bit grayscale and virtually stacked in 3 dimensions using the Amira software package (50). For automated tracing of individual collagen fibers, we modified the previously described techniques developed for electron tomography (51,52), which were packaged into the XTracing filament detection extension available for Amira (50). In brief, this tracing algorithm consists of 2 main steps: template matching and a line search approach. Template matching uses a graphics processing unit (NVIDIA Quadro M2000, Santa Clara, California) to compute the voxel cross-correlation field in a 3-dimensional image stack, with a cylindrical template that mimics a collagen fiber segment with a mask radius of 5 μm and a length of 20 μm. The line search approach identifies the voxels that form the centerline of each collagen fiber. From an initial seed point, a search cone spanning 20 μm and 45 degrees identifies candidate collagen fiber points that are scored for continuity, curvature, and deviations from the orientation field. The line search stops when the search cone fails to identify candidate points with scores above the minimum threshold.

CHARACTERIZATION OF THE COLLAGEN FIBER ORIENTATION AND MICROSTRUCTURE. Each collagen fiber was evaluated with respect to orientation and undulation. Two angles were used to define the fiber orientation. The azimuthal angle (φ) refers to the angle from the positive radial axis of the fiber's projection on the longitudinal-radial plane, where $\varphi = 0$ degrees is then the radial direction. The elevation angle (ϑ) refers to the angle from the positive circumferential axis of the fiber's projection on the circumferential-longitudinal plane, where $\vartheta = 0$ degrees and $\vartheta = 90^\circ$ correspond to the circumferential and longitudinal directions, respectively. Fiber undulation (u) is defined as the ratio between the path length (l_p) and the end-to-end length (l_e) of a given fiber.

$$u = \frac{l_p}{l_e} \quad \text{(Eq. 7)}$$

LV MYOCARDIAL COLLAGEN CONTENT BY LIGHT MICROSCOPY. LV myocardial collagen content in lateral free-wall sections was analyzed in subset of the referent control (n = 9), 4 weeks post-LVPO (n = 6), and 5 weeks post-LVPO (n = 7) pigs. Collagen was visualized via picrosirius red staining under polarized light at a magnification of 40×. Viewing fields were chosen at random from the LV epicardium, mid-myocardium, and endocardium. Fields with large blood vessels were excluded from the analysis. Collagen content was calculated as the percentage of positively stained area in the field of view (ImageJ software) (53).

PLASMA N-TERMINAL PRO-BRAIN NATRIURETIC PEPTIDE. Plasma samples were obtained in a subset of the 4 weeks post-LVPO (n = 8) and 5 weeks post-LVPO (n = 8) pigs, as well as a referent control group that included pigs from a previous study (n = 19) (54). Plasma was thawed on ice and diluted 1:10 with phosphate-buffered saline. Pig-specific N-terminal pro-brain natriuretic peptide (NT-

FIGURE 1 LVPO-Induced LV Hypertrophy

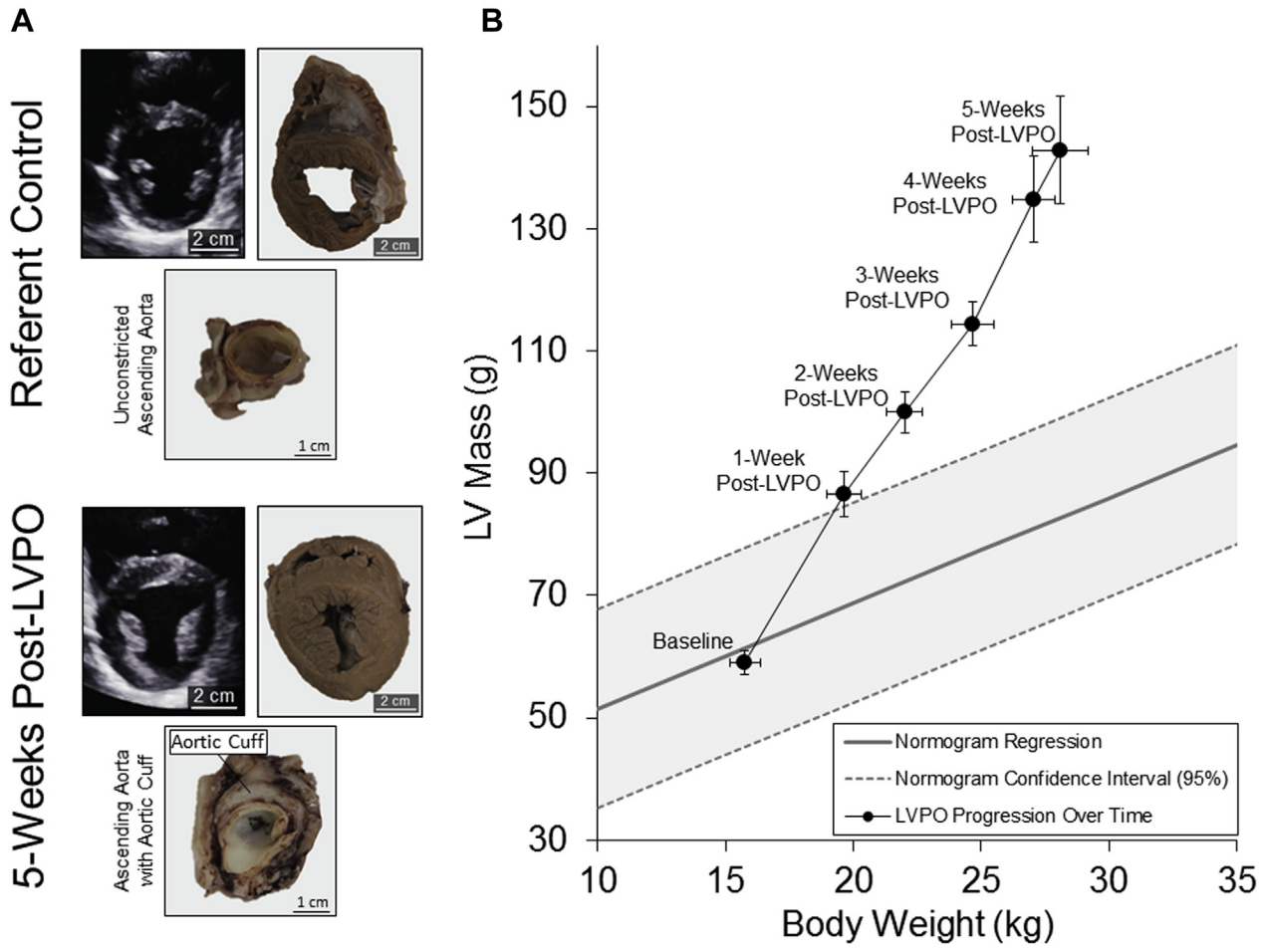

(A) Representative transthoracic echocardiographic views of the left ventricular (LV) short-axis at the level of the papillary muscle, along with preserved bisections of the intact ventricles and ascending aorta. A clear and obvious thickening of the LV wall occurred as a result of LV pressure overload (LVPO). The aortic cuff significantly reduced the cross-sectional area of the aortic lumen. **(B)** LV mass relative to body weight obtained at baseline and during 5 weeks post-LVPO superimposed on a normogram of this relation developed from previous studies. The observed increase in LV mass relative to body weight indicates an LVPO-induced hypertrophic response. (baseline – 4 weeks post-LVPO: n = 14; 5 weeks post-LVPO: n = 7)

proBNP) was measured using an enzyme-linked immunoassay format (Kamiya Biomedical Company, Seattle, Washington).

TARGETED GENE EXPRESSION. Targeted mRNA levels for the calcium regulatory proteins sarcoplasmic reticulum calcium adenosine triphosphatase and phospholamban were measured (55,56), as well as the cytoskeletal protein titin (57,58). Briefly, RNA was extracted from LV mid-myocardium (RNeasy Fibrous Tissue Mini Kit, Qiagen, Valencia, California), and the quality and concentration confirmed (Experion Automated Electrophoresis System, Bio-Rad, Hercules, California). RNA samples were then converted to cDNA (RT2 First Strand Kit, Qiagen, Cat. #330401, Valencia, California) and quantitative real-time polymerase chain reaction (qPCR) was performed (RT2 qPCR Primer Assay, Qiagen Cat. #33001) with pig-specific mRNA expression primers (Qiagen). The qPCR reactions (Bio-Rad CFX96) were carried out using cycling parameters designated by the manufacturer. Cycle time (Ct) values of the mean for *Gapdh* were used as reference gene values for normalization.

FIGURE 2 **Echocardiographic Indices**

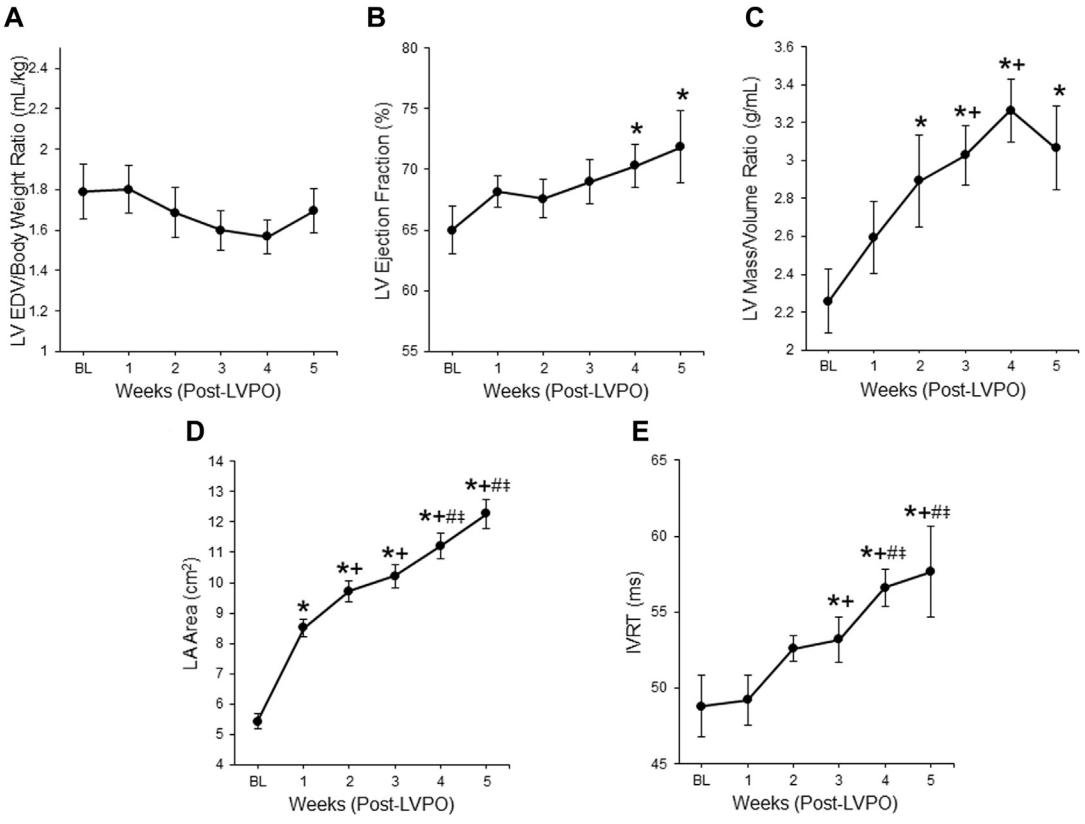

Baseline values of **(A)** LV end-diastolic volume (LVEDV)/body weight ratio and **(B)** LV ejection fraction were largely maintained during 5 weeks post-LVPO, whereas **(C)** LV mass/volume ratio, **(D)** left atrial (LA) area, and **(E)** isovolumic relaxation time (IVRT) progressively increased. *p < 0.05 versus baseline value; +p < 0.05 versus 1-week value; #p < 0.05 versus 2-week value; ‡p < 0.05 versus 3-week value. (baseline – 4 weeks post-LVPO: n = 14; 5 weeks post-LVPO: n = 7). Abbreviations as in Figure 1.

Fold-change expression was calculated using the ΔΔCt method, in which 2-ΔΔCt is the fold-change value.

STATISTICAL ANALYSIS. Data are reported as the mean ± SEM. Comparative analyses were performed using a 1-way analysis of variance followed by post hoc pairwise comparisons using the least significant difference method. For the assessment of the relative change from baseline, a Student's *t*-test was performed in which significance of the transformed data were determined using a null hypothesis of a zero mean value. For SHG-based collagen fiber characterization, at each timepoint, all values of φ, ϑ, and u were pooled and binned into 100 equally sized bins. The resulting frequency distributions were subjected to a Kruskal-Wallis 1-way analysis of variance for nonparametric comparisons across different timepoints. A multiple linear regression model with inputs derived at 1 week post-LVPO was used to predict the relative change in K_C^* at 2, 3, 4, and 5 weeks post-LVPO, and the p value and *t*-statistic were calculated for each of the input variables. Spearman's rank correlation analysis was used to interrelate experimental response variables at 4 and 5 weeks post-LVPO. All statistical analyses were performed with SPSS software version 24.0 (IBM, Armonk, New York),

TABLE 1 LV Function and Biochemistry With Progressive LVPO

	Referent Control	4 Weeks Post-LVPO	5 Weeks Post-LVPO
LV pressures			
Peak-systolic pressure (mm Hg)	117 ± 5	149 ± 14*	153± 7*
End-diastolic pressure (mm Hg)	7.4 ± 0.7	12.5 ± 0.6*	12.5 ± 0.9*
LV systolic function			
Stroke work (kg/cm)	4.6 ± 0.5	7.0 ± 0.6*	7.9 ± 0.6*
PRSW (g/cm^2)	37.3 ± 8.7	88.9 ± 11.4*	88.5 ± 12.7*
Max +dP/dt (mm Hg/s)	2,165 ± 431	2,096 ± 867	1,194 ± 131
Normalized max +dP/dt† (1/s)	18.5 ± 3.9	13.1 ± 4.2	7.8 ± 0.8
End-systolic elastance (mm Hg/ml)	1.3 ± 0.3	3.9 ± 1.0*	3.3 ± 1.1*
Normalized end-systolic elastance‡ (mm Hg/ml/g)	0.016 ± 0.005	0.028 ± 0.008	0.024 ± 0.01
LV diastolic function			
Max −dP/dt (mm Hg/s)	2,168 ± 385	1,356 ± 177	1,371 ± 108
Normalized max −dP/dt† (1/s)	18.3 ± 2.9	9.0 ± 0.5*	8.9 ± 0.3*
Tau (ms)	25.3 ± 2.5	32.6 ± 2.0	34.7 ± 2.6*
Biochemistry			
Plasma NT-proBNP (pg/ml)	604 ± 63	676 ± 68	1347 ± 497*,‖
SERCA (mRNA)§	–	1.1 ± 0.2	1.1 ± 0.1
Phospholamban† (mRNA)§	–	1.2 ± 0.2	1.5 ± 0.4
Titin (mRNA)§	–	1.2 ± 0.1	1.8 ± 0.3*,‖

Values are mean ± SD. Sample sizes are n = 4 or greater/group; see Methods for details. *p < 0.05 vs. referent control. †Normalized by peak left ventricular (LV) systolic pressure. ‡Normalized by LV mass. §Results expressed as $2^{-\Delta\Delta CT}$ fold change. ‖p < 0.05 vs. 4 weeks post-left ventricular pressure overload (LVPO).

NT-proBNP = N-terminal pro–brain natriuretic peptide; PRSW = pre-load recruitable stroke work; SERCA = sarcoplasmic reticulum calcium adenosine triphosphatase.

R version 3.6.3 (The R Foundation, Vienna, Austria), or MATLAB (version R2018a, The MathWorks Inc, Natick, Massachusetts). A p value of <0.05 was considered statistically significant.

RESULTS

LV GEOMETRY AND FUNCTION. LVPO induced a monotonic increase in LV mass exceeding normal developmental growth by 2 weeks post-LVPO with a relative doubling of LV mass at 5 weeks post-LVPO (Figure 1). In contrast, the LV EDV/body weight ratio was preserved, and LVEF was modestly increased post-LVPO (Figures 2A and 2B). LV mass/volume ratio increased by 2 weeks post-LVPO (Figure 2C), whereas LA area more than doubled by 5 weeks post-LVPO (Figure 2D). In comparison, LA area of age-matched referent control pigs (5.7 ± 0.6 cm^2) was unchanged with respect to the baseline value (5.4 ± 0.4 cm^2). Thus, with LVPO, significant LV hypertrophy and LA dilation occurred over and above that of normal growth.

As expected, LV peak systolic pressure was increased at 4 and 5 weeks post-LVPO (Table 1). Additional indexes of LV pump function (LVEF shown in Figure 2B), such as stroke work and LV pressure development (+dP/dt), either increased or remained unchanged from the referent control values (Table 1). Load-independent indexes of LV function such as pre-load recruitable stroke work (PRSW) and end-systolic elastance followed a similar pattern (Table 1). LV end-diastolic pressure was increased from referent control values at 4 and 5 weeks post-LVPO (Table 1) and paralleled the relative magnitude in LA area at these timepoints (Figure 2D). Indexes of active LV relaxation were impaired with progressive LVPO, which included prolongation of IVRT (Figure 2E). Other indexes of LV relaxation derived from invasive LV pressure measurements, such as peak negative pressure development and tau, were both changed from referent control values by 5 weeks post-LVPO (Table 1). Thus, in this model of progressive LVPO, LV systolic function was not compromised. However, indexes of LV diastolic function were significantly affected, which is consistent with the functional phenotype of HFpEF (27,49,59).

LV BIOMECHANICAL FUNCTION. LV peak myocardial strain in the circumferential direction was generally retained post-LVPO, whereas slight initial (1 week post-LVPO) increases remained unchanged by 5 weeks post-LVPO (Figure 3A). In the longitudinal direction, LV peak myocardial strain was preserved or moderately elevated throughout the LV myocardium with significant elevations occurring in only the endocardial layer (Figure 3A). Thus, similar to indexes of LV systolic function (Table 1), LV peak strain patterns were not diminished by LVPO.

LV diastolic myocardial strain rate was largely preserved in the circumferential direction, but monotonically declined in the longitudinal direction, with significant reductions in the LV epicardium and mid-myocardium by 3 and 4 weeks post-LVPO, respectively (Figure 3B). Mean LV diastolic myocardial stiffness ($|\kappa_{MR}|$), taken as the average value among all regions, significantly increased by 4 weeks post-LVPO in the circumferential direction and by 2 weeks post-LVPO in the longitudinal direction. Mean κ_{MR} in the circumferential direction exhibited a significant late elevation with an approximate 30% increase occurring between 4 and 5 weeks post-LVPO (Figure 3C). Regional measurements of κ_{MR} determined via STE exhibited significant correlation with analogous measurements obtained from invasive catheterization ($\rho = 0.70$, $p = 0.024$), supporting the use of STE for serial evaluation of LV myocardial mechanical properties.

LV CHAMBER STIFFNESS. LV pressure-volume relations were notably altered post-LVPO, including

FIGURE 3 **LV Myocardial Mechanical Response and Mechanical Properties**

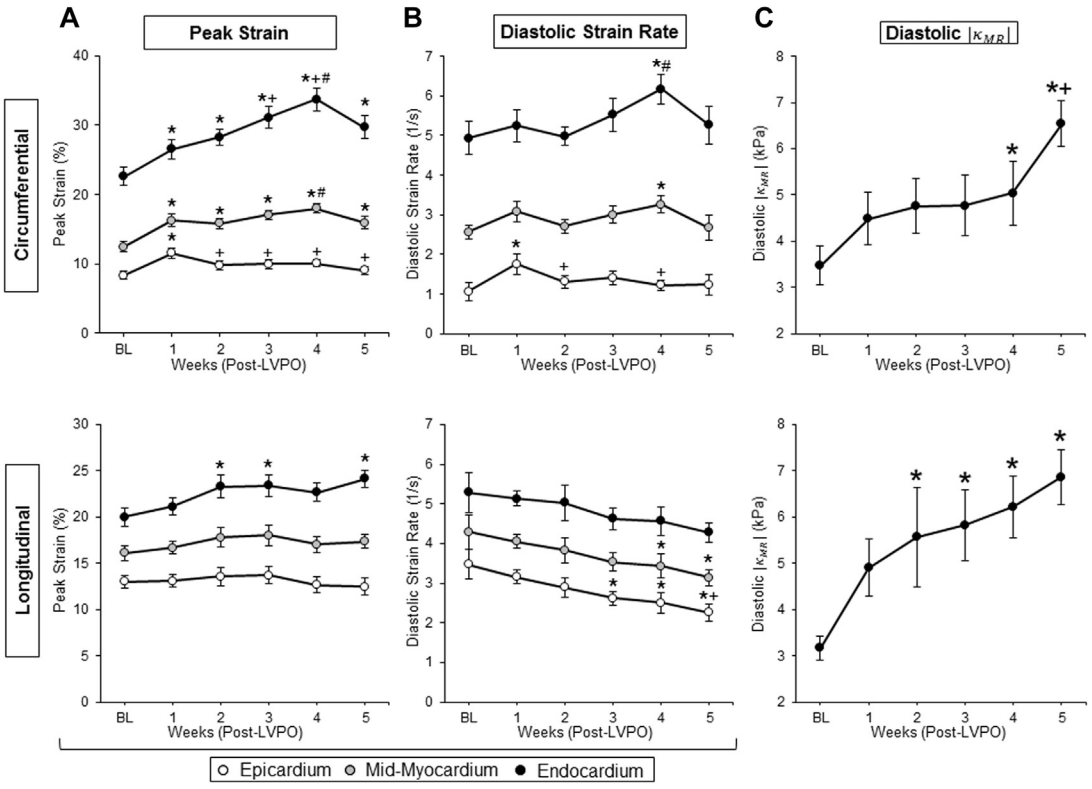

(A) Peak LV myocardial strain and **(B)** diastolic strain rate underwent similar changes in the epicardium, mid-myocardium, and endocardium during 5 weeks post-LVPO. **(C)** The mean diastolic LV myocardial stiffness (average of obtained regional stiffness values) progressively increased during 5 weeks post-LVPO in both the circumferential and longitudinal directions. *p $<$ 0.05 versus baseline value; +p $<$ 0.05 versus 1-week value; #p $<$ 0.05 versus 2-week value. (baseline – 4 weeks post-LVPO: n = 14; 5 weeks post-LVPO: n = 7). Abbreviations as in Figure 1.

changes in the diastolic phase (Figure 4A). At 5 weeks post-LVPO, significant increases in LV chamber stiffness relative to referent control values were indicated by changes in both K_C and K_C^* (Figure 4B). A steady rise in K_C^* resulted in a doubling of the baseline value by 5 weeks post-LVPO, with a significant late rise occurring between 4 and 5 weeks post-LVPO (Figure 4C). There was significant correlation between K_C and K_C^* (ρ = 0.75, p = 0.013) that supported the use of K_C^* for serial evaluation of LV chamber stiffness. Thus, the progressive rise in LV chamber stiffness, which is considered a key determinant of HFpEF progression (32,59), occurred post-LVPO and could be noninvasively monitored.

LV MYOCARDIAL COLLAGEN CONTENT AND ORGANIZATION. LV myocardial collagen content increased in the epicardium, mid-myocardium, and endocardium by 4 weeks post-LVPO with no further elevations observed at 5 weeks post-LVPO (Figure 5). Layer-specific differences in myocardial collagen content emerged at 5 weeks post-LVPO, with significantly greater content in the endocardium compared with the epicardium. The increased collagen content post-LVPO was coupled with changes in collagen fiber microstructure (Figure 6A). In all 3 LV myocardial layers, collagen fiber undulation distributions indicated a significantly higher coincidence of less undulated collagen fibers at 5 weeks post-LVPO, with significant changes occurring between 4 and 5 weeks

FIGURE 4 Evaluation of LV Chamber Stiffness

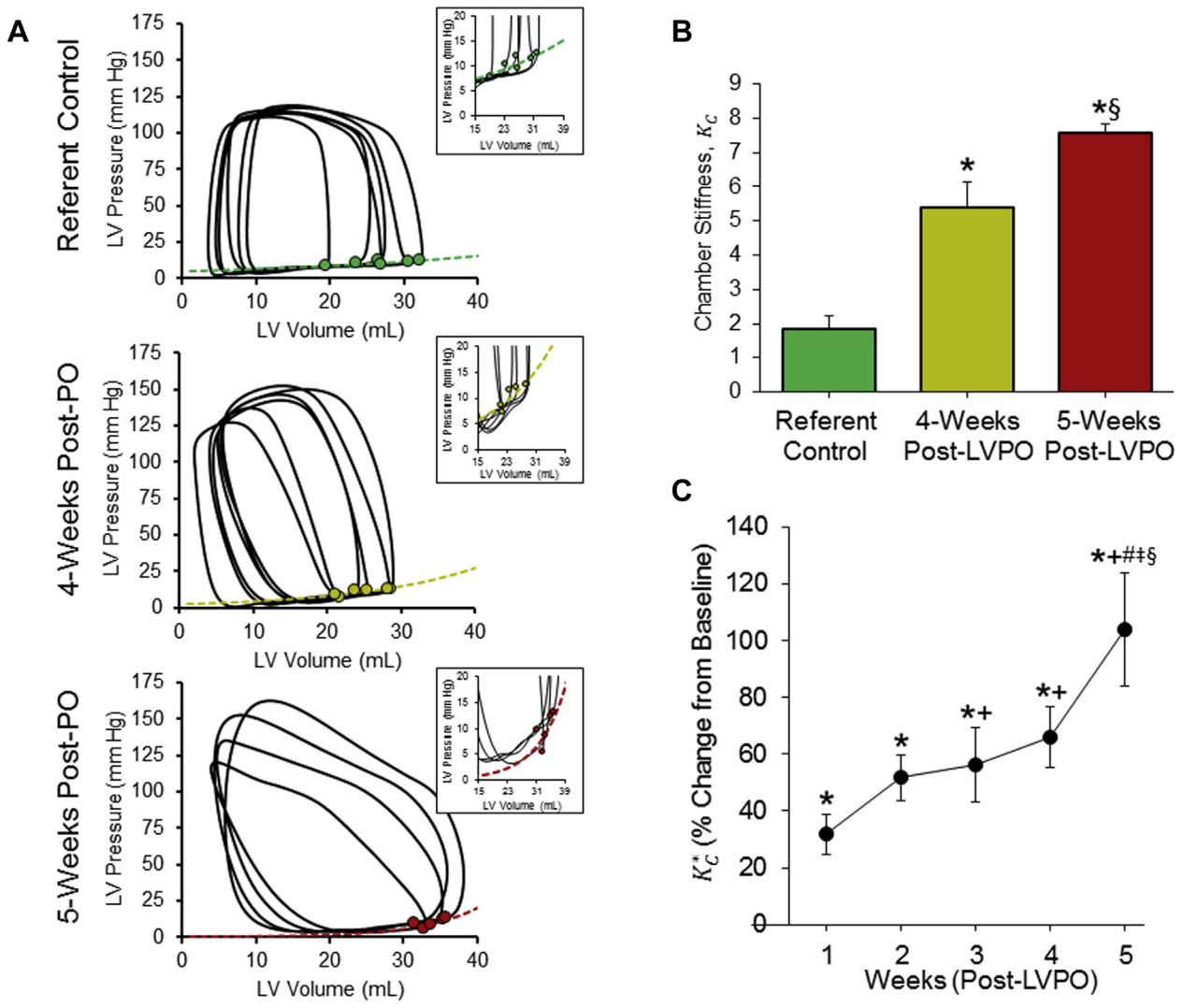

(A) Representative pressure-volume relations developed from invasive LV pressure measurements. **(B)** Generated pressure-volume loops from a subset of referent control (n = 6), 4 weeks post-LVPO (n = 4), and 5 weeks post-LVPO (n = 4) pigs were used to derive LV chamber stiffness (*Kc*), which exhibits significant and late (4 weeks post-LVPO vs. 5 weeks post-LVPO) increases with LVPO. **(C)** A noninvasive surrogate (K_C^*) was used for serial assessment of LV chamber stiffness, demonstrating a similar late elevation (4 weeks post-LVPO vs. 5 weeks post-LVPO) as well as progressive LV chamber stiffening during 5 weeks post-LVPO. *p < 0.05 versus baseline value; +p < 0.05 versus 1-week value; #p < 0.05 versus 2-weeks value; ‡p < 0.05 versus 3-week value; §p < 0.05 versus 4 weeks value. (baseline – 4 weeks post-LVPO: n = 14; versus weeks post-LVPO: n = 7). Abbreviations as in Figure 1.

post-LVPO in the endocardial and epicardial layers (Figure 6B). In terms of collagen fiber organization, collagen fiber angle distributions on the circumferential-longitudinal plane in the endocardium and epicardium were significantly shifted toward the circumferential axis by 4 and 5 weeks post-LVPO, respectively (Figure 6C). Collagen fiber angle distributions on the radial-longitudinal plane were generally preserved post-LVPO (Figure 6D). Thus, although total collagen content increased at both 4 and 5 weeks post-LVPO, shifts in fibrillary collagen architecture occurred at 5 weeks post-LVPO and were coincident with the significant rise in LV chamber stiffness.

BIOCHEMICAL MARKERS. Plasma NT-ProBNP levels were maintained at referent control values at 4 weeks post-LVPO but increased significantly at 5 weeks post-LVPO. LV myocardial mRNA levels for

FIGURE 5 Quantification of LV Myocardial Collagen Content

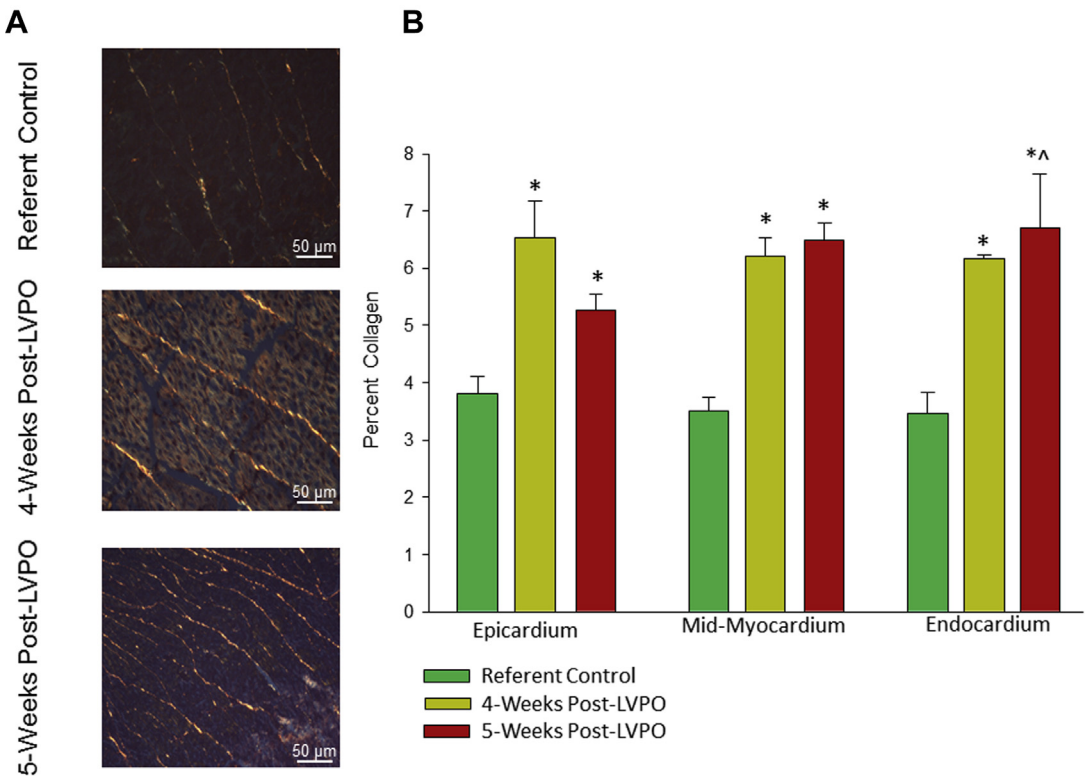

(A) Transmural sections of the LV myocardium were stained with picrosirius red and imaged at 40× magnification. These images from the mid-myocardium reflect the increased fibrillar collagen content that occurred with LVPO. (B) Percent collagen content was computed for samples corresponding to the endocardium, mid-myocardium, and epicardium for referent controls (n = 9), 4 weeks post-LVPO (n = 6), and 5 weeks post-LVPO (n = 7). *p < 0.05 versus referent control endocardium, mid-myocardium, and epicardium, ^p < 0.05 versus 5-week epicardium. Abbreviations as in Figure 1.

sarcoplasmic reticulum calcium adenosine triphosphatase and phospholamban were unchanged at 4 or 5 weeks post-LVPO (Table 1). The cytoskeletal protein titin, which was previously shown to be increased with LVPO and HFpEF (58) was increased by 5 weeks post-LVPO (Table 1).

PREDICTING CHANGES IN LV CHAMBER STIFFNESS. To examine the relationship between LVPO-induced regional changes in κ_{MR} and LV wall thickness (H), we computed the slope of a linear regression between these response variables ($\partial K_{MR}/\partial H$), which was developed with measurements from the 6 defined LV myocardial regions at 1 week post-LVPO. When considered as a composite, changes in regional κ_{MR} and H were significantly correlated, whereas $\partial K_{MR}/\partial H$ was negative (Figure 7A). Individual values for $\partial K_{MR}/\partial H$, along with the LV chamber stiffness determined at 1 week post-LVPO ($K^*_{C,1-week}$), were incorporated into a multiple linear regression model of the form

$$K^*_{C,pred.} = a\frac{\partial K_{MR}}{\partial H} + bK^*_{C,1-week} + cT + d \qquad \text{(Eq. 7)}$$

where $K^*_{C,pred.}$ is the predicted percent increase in chamber stiffness at time T (post-LVPO time, in days), and a, b, c, and d are fitting parameters. The regression model, built with data from 2 weeks post-LVPO through 5 weeks post-LVPO, yielded a strong linear relation between $K^*_{C,pred.}$ and K^*_C (Figure 7B), with all model fitting parameters (a, b, c, and d) exhibiting statistical significance ($p < 0.050$). A repeated measures (rm) correlation analysis was performed to account for the within-individual association for paired measures, with a positive correlation coefficient between $K^*_{C,pred.}$ and K^*_C ($\rho rm = 0.42$, $p = 0.011$) (60). Furthermore, a linear mixed model was generated, and a Bonferroni adjustment revealed pairwise

FIGURE 6 Characterization of Collagen Fiber Structure and Orientation

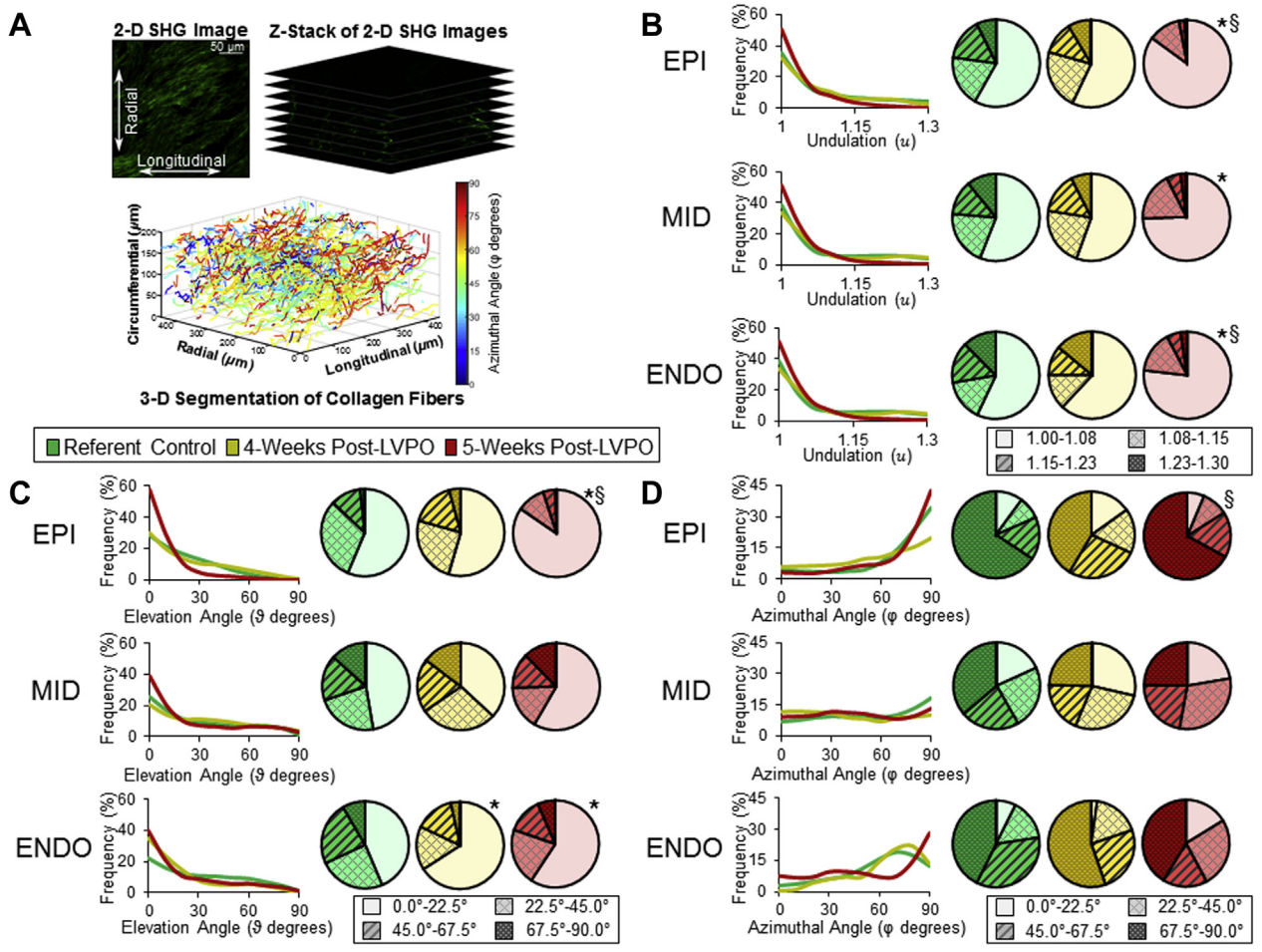

(A) Three-dimensional (3-D) stacks of 2-dimensional (2-D) images acquired from second harmonic generation (SHG)–enabled reconstruction of collagen fibers and subsequent representation as vectors in a Cartesian coordinate system for samples corresponding to referent controls (n = 5), 4 weeks post-LVPO (n = 6), and 5 weeks post-LVPO (n = 7). **(B)** Regional fiber undulation (u) distributions were computed for the epicardium (EPI), mid-myocardium (MID), and endocardium (ENDO) based on reconstructed fiber geometries. Two fiber-specific angles were computed to quantify fiber orientation. **(C)** The elevation angle, ϑ, was computed from the circumferential-longitudinal plane. An angle of $\vartheta = 0^{\circ}$ indicates fiber alignment with the circumferential axis. **(D)** The azimuthal angle, φ, was computed from the longitudinal-radial plane. An angle of $\varphi = 0^{\circ}$ indicates fiber alignment with the radial axis. *$p < 0.05$ versus referent control value; §$p < 0.05$ versus 4-week value. Other abbreviation as in Figure 1.

significant statistical differences between the predicted values at all 4 timepoints.

CORRELATION BETWEEN LV MYOCARDIAL COMPOSITION AND BIOMECHANICS. A correlation matrix was developed to relate the relative change in LV biomechanical response variables and geometrical, compositional, and microstructural features of the LV myocardium (Figure 8). LV wall thickness and myocardial collagen content were not correlated to biomechanical measurements, whereas some changes in matrix microstructure were associated with these measurements. Specifically, a reduction in collagen fiber undulation ($u \rightarrow 1$) was correlated with increased LV myocardial stiffness in all 3 layers of the LV. Furthermore, an inverse correlation was observed between the collagen fiber elevation angle and LV myocardial stiffness in the epicardial layer, linking a preferential fiber orientation toward the circumferential axis ($\vartheta \rightarrow 0^{\circ}$) to higher circumferential LV myocardial stiffness.

FIGURE 7 **Predicting LVPO-Induced Increase in LV Chamber Stiffness Based on Early Noninvasive Measurements**

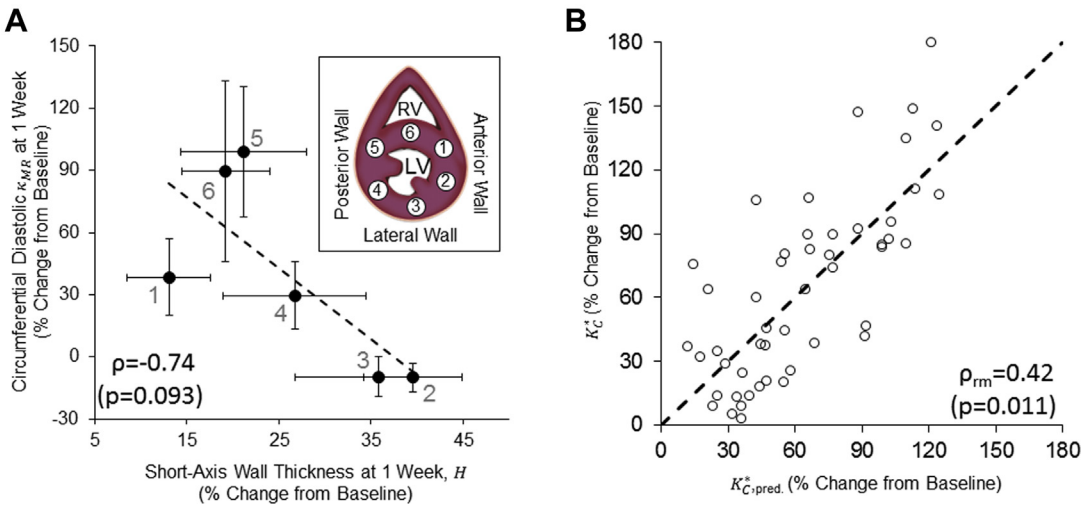

(A) Region-matched changes in wall thickness (H) and circumferential diastolic myocardial stiffness (κ_{MR}) obtained at 1 week post-LVPO exhibited an inverse correlation among all post-LVPO animals (n = 14). **(B)** Predicted values for LVPO-induced changes in LV chamber stiffness relative to baseline ($K_{C,\,pred.}^*$) were generated through multiple linear regression modeling. $K_{C,\,pred.}^*$ significantly correlated with experimental values, suggesting that noninvasive measurements obtained at 1 week post-LVPO can predict the severity of subsequent LV chamber stiffening. RV = right ventricular; other abbreviations as in Figure 1.

FIGURE 8 **Biomechanical, Geometrical, Compositional, and Microstructural Correlations**

		Peak Strain (%)	Diastolic Strain Rate (1/s)	Diastolic κ_{MR} (kPa)
Thickness (mm)		0.17	0.35	0.34
CVF (%)		-0.08	-0.04	0.32
u	EPI	0.19	0.07	-0.68 *
	MID	0.45	0.24	-0.58 *
	ENDO	0.24	0.22	-0.57 *
ϑ (deg)	EPI	0.32	0.32	-0.62 *
	MID	0.40	0.27	-0.48
	ENDO	0.29	0.06	-0.35
φ (deg)	EPI	-0.07	-0.03	0.13
	MID	0.24	0.18	-0.35
	ENDO	0.12	0.19	-0.29

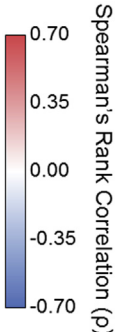

A Spearman's rank correlation analysis was used to interrelate region-matched biomechanical response variables [peak strain, diastolic strain rate, and diastolic myocardial stiffness (κ_{MR}) with geometrical (wall thickness), compositional (collagen content), and microstructural [collagen undulation (u)], and orientation (ϑ and φ) response variables. All correlations refer to data means at the terminal study timepoints; (4 weeks post-LVPO: n = 6; 5 weeks post-LVPO: n = 7). *p < 0.05 for Spearman's rank correlation coefficient (ρ). Abbreviations as in Figures 1 and 6.

DISCUSSION

HFpEF is a specific HF phenotype that afflicts millions of patients annually, although specific and effective therapeutic strategies have not been forthcoming (1,2,61). This issue is also compounded by the fact that the indexes of LV function that contribute to the development and progression of HFpEF require specific measures of LV myocardial diastolic performance (20,21). The present study addressed these issues by using a large animal model of progressive LVPO, which over time, recapitulated many of the key phenotypical features of HFpEF. The significant findings from this study are 3-fold. First, progressive LVPO induced a gradual and significant rise in LV diastolic myocardial stiffness, which was noninvasively determined and thus holds potential for clinical assessment of HFpEF. Second, these LVPO-induced elevations in LV diastolic myocardial stiffness appeared not only to be modulated by myocardial collagen content, but also by changes in collagen microarchitecture (shifts in alignment and undulation). Third, our data suggested that with LVPO, a relationship between early changes in regional LV diastolic myocardial stiffness and LV wall thickness could be predictive of the subsequent rise in LV chamber stiffness. Taken together, these novel findings elucidated the effects of LVPO on LV myocardial biomechanics and hold promise as a translational approach to monitor and predict HFpEF progression as well as evaluating new therapeutic targets.

LV MYOCARDIAL BIOMECHANICS. LV longitudinal myocardial strain has been used as a clinical index for HF diagnosis and phenotyping, wherein changes in global values are indicative of LV systolic function, and changes in regional strain patterns can provide information for HF sub-classification (62–65). Although past clinical studies suggested that HFpEF is accompanied by a reduction in LV global longitudinal myocardial strain, the present study (along with others) observed modest, if any, early changes in regional or global myocardial strain and diastolic strain rate (27,29,62,66–68). In addition to LV regional strain measurements, the present study examined several indexes of LV systolic function. Overall, these measurements, such as EF and stroke work, were either preserved or modestly changed with progressive LVPO. Load-independent measures of LV function, such as PRSW and end-systolic elastance, followed a similar trend. Thus, using multiple approaches, this model of LVPO was shown to not to be associated with a compromise in LV pump function or systolic performance. The relative increase in load-independent indexes of LV function, such as PRSW, were likely due to the increased LV mass, and as such, increased mass of contractile units. Furthermore, at the timepoints measured in this study, LVPO was not associated with transcriptional shifts in key determinants of sarcoplasmic reticular Ca+2 function. Thus, this progressive LVPO model appeared to initially present overall with intact LV myocardial contractile function, with clear declines in both active and passive components of LV diastolic function, which is a key functional feature of HFpEF.

With progressive LVPO and LV hypertrophy, other key characteristics of HFpEF development occurred, including LA dilation, increased LV diastolic pressure, and elevated NT-proBNP. From a biomechanical perspective, hypertrophy is the primary adaptive response of the LV myocardium to LVPO, mitigating the elevated values LV myocardial wall stress (67). Partially as a result of LV hypertrophy, we observed progressive and significant elevations in K_C^* with LVPO, similar to previous reports (22,30–32,68,69). Our serial analyses enabled novel comparison of late study timepoints (4 weeks post-LVPO vs. 5 weeks post-LVPO), which suggested that late K_C^* elevations were not solely governed by LV myocardial collagen accumulation (i.e., "fibrosis") but also the local changes in LV myocardial mechanical properties as reflected by κ_{MR}. However, it must be recognized that changes in LV chamber stiffness are governed by both active relaxation as well as passive myocardial compliance. In the present study, a prolongation of both IVRT and tau occurred at the LVPO timepoints, which were indicative of changes in active relaxation. Thus, it is likely that the rise in LV chamber stiffness with LVPO was due to both changes in LV myocardial collagen content and structure, as well as active relaxation.

Although the co-dependence of aberrant LV structural mechanics on both LV geometry and myocardial mechanical properties is expected in all modes of HF, these results provided novel directional and regional detail on LVPO-induced elevations in κ_{MR}, and importantly, informed temporal relation to elevations in K_C^* (22,68,70–72). Specifically, late LVPO-induced elevations in κ_{MR} were coupled with an abrupt rise in K_C^*, which suggested that image-based determination of LV myocardial mechanical properties holds

potential usefulness to identify a key transition point and progression of HFpEF.

MICROSTRUCTURAL CHANGES IN THE LV MYOCARDIUM WITH LVPO. One of the hallmarks of the LV myocardial remodeling with LVPO is increased fibrillar collagen content, which is due in part to shifts in collagen synthesis and turnover. Moreover, these changes in LV myocardial collagen content with LVPO contributed to diastolic dysfunction and were not readily reversible (73–77). Specifically, increased LV myocardial collagen content was associated with increased LV chamber stiffness and LV myocardial stiffness (78–81). In the present study, a correlation between LV myocardial stiffness and collagen content with progressive LVPO was observed, but our studies moved beyond this observation. Specifically, our analysis identified that changes in collagen fiber undulation and orientation, which are the key microstructural features that govern collagen engagement in load-bearing, were also associated with changes in LV myocardial stiffness at late LVPO timepoints (82). Moreover, the late emergence of coinciding, layer-specific differences in LV myocardial collagen content and fiber undulation distributions further suggested that both factors contributed to increased passive LV myocardial stiffness with LVPO.

The present study also identified that LV myocardial collagen fiber realignment occurred as a function of time with LVPO, which further supported the concept that the microarchitecture of the assembled collagen fibers with LVPO was abnormal. However, it must be recognized that past studies with LVPO identified significant shifts in myocyte cytoarchitecture, such as titin, which were associated with changes in LV myocardial stiffness properties (83). Although examined only at the transcriptional level, the present study identified that titin mRNA was increased at the late (5 weeks) post-LVPO timepoint. Thus, shifts in titin content and potentially phosphorylation states might have occurred in this LVPO model and warrant future study (83). Although due to a different LV remodeling stimulus, recent findings identified a similar shift in collagen microarchitecture within the hypertrophied remote region in the post-infarcted LV myocardium (84). When coupled with the significant late increase in κ_{MR} in the circumferential direction, our findings suggested that LV myocardial collagen fiber realignment was a key factor underlying increased LV myocardial stiffness with LVPO and was an independent and/or additive mechanism that contributed to the progression of HFpEF.

PREDICTING LATE INCREASES IN LV CHAMBER STIFFNESS DUE TO LVPO. In general, muscle growth and remodeling are adaptive, cell-mediated processes that restore local mechanical homeostasis (i.e., baseline values of stresses and strains) under sustained deviations in mechanical loading (85–89). Thus, elevations in local stress result in a compensatory increase in mass while stress reductions result in the opposite. Using the present study as a platform, we postulated that if growth and remodeling processes also act to retain normal structure function relations at the LV chamber level (i.e., LV chamber stiffness), then LV mass changes must be coupled with opposing changes in LV myocardial stiffness. At 1 week post-LVPO, increased regional LV wall thickness was inversely correlated to regional changes in κ_{MR}. Using this observation as a framework, we then examined the relation between early changes in regional LV wall thickness and κ_{MR} with LVPO and identified a predictive model of K_C^* elevations over later post-LVPO timepoints. This image-based biophysical analysis has the potential to yield a clinically relevant approach to predict the rate and extent of increased LV chamber stiffness with prolonged LVPO, and hence, the relative risk for HFpEF. Defining early determinants for the risk of developing HFpEF have been identified as an important area of development for disease management (33–37).

STUDY LIMITATIONS. Although the present study identified unique ultrastructural and regional biophysical relationships in a large animal model of LVPO, several limitations should be recognized. Although indexes of LV diastolic function (i.e., LA area, IVRT, tau, LV chamber stiffness) suggest that the LVPO pigs were on a trajectory to develop symptomatic HFpEF (e.g., pulmonary edema), these longitudinal studies were not carried out to this endpoint. However, by 5 weeks post-LVPO, a biomarker feature for the progression to HF was identified by increased NT-proBNP (90). As such, this LVPO model appeared to meet the criteria for emulating key features of the natural history of the progression to HFpEF. Because of the inherent sensitivity of indexes of LV diastolic function to measurements of LV filling pressure, it must be recognized that our analysis was limited by the estimations of LV pressures that were used at both the onset of diastole and end-diastole. Future work will

focus on developing new methods of characterizing LV filling pressure in a serial manner and incorporating those measurements into this analytical framework.

CONCLUSIONS

The present study, using STE, provided a serial method for assessing regional LV myocardial stiffness, but future work will be required to examine whether and to what degree these measurements are sensitive to and predictive of pharmacotherapies. Past studies have identified that in isolated myocyte preparations, passive stiffness properties are affected with LVPO (91). In light of the fact that steady-state mRNA levels for the cytoskeletal protein titin increased at the late LVPO timepoints, these myocyte based studies would be an appropriate future direction. These limitations notwithstanding, the unique findings from this study were that assessment of global changes in LV function with LVPO might be insensitive to identifying key transition points in HFpEF development and that quantifying the relative fibrosis through LV myocardial collagen content alone was insufficient to identify the mechanistic underpinnings that govern increases in LV myocardial stiffness and LV chamber stiffness, which are biophysical milestones of this disease.

ADDRESS FOR CORRESPONDENCE: Dr. Francis G. Spinale, University of South Carolina School of Medicine, 6439 Garners Ferry Road, Building 3, Room 234, Columbia, South Carolina 29209. E-mail: cvctrc@uscmed.sc.edu.

PERSPECTIVES

COMPETENCY IN MEDICAL KNOWLEDGE: The underlying mechanisms that contribute to the development and progression of HFpEF remain incompletely understood. This is due in part to a paucity of animal models that recapitulate key phenotype features of HFpEF, which can be measured in a serial fashion. The present study developed a pig model of progressive PO, which developed into HFpEF phenotype. Key biophysical parameters such as collagen microstructure and regional stiffness were associated with the transition to the HFpEF phenotype. Early changes in regional myocardial stiffness predicted the extent of the HFpEF phenotype.

TRANSLATIONAL OUTLOOK: This study provides the foundation by which new directions in diagnostics and therapeutics can be developed.

REFERENCES

1. Benjamin EJ, Blaha MJ, Chiuve SE, et al. Heart disease and stroke statistics'2017 update: a report from the American Heart Association. Circulation 2017;35:e146–603.

2. Bursi F, Weston SA, Redfield MM, et al. Systolic and diastolic heart failure in the community. JAMA 2006;296:2209–16.

3. Bronzwaer JGF, Paulus WJ. Diastolic and systolic heart failure: different stages or distinct phenotypes of the heart failure syndrome? Curr Heart Fail Rep 2009;6:281–6.

4. Komajda M, Carson PE, Hetzel S, et al. Factors associated with outcome in heart failure with preserved ejection fraction: findings from the Irbesartan in Heart Failure with Preserved Ejection Fraction Study (I-PRESERVE). Circ Heart Fail 2011; 4:27–35.

5. Zile MR, Gaasch WH, Anand IS, et al. Mode of death in patients with heart failure and a preserved ejection fraction: results from the irbesartan in heart failure with preserved ejection fraction study (I-Preserve) Trial. Circulation 2010; 121:1393–405.

6. Yusuf S, Pfeffer MA, Swedberg K, et al. Effects of candesartan in patients with chronic heart failure and preserved left-ventricular ejection fraction: The CHARM-Preserved trial. Lancet 2003; 362:777–81.

7. Ahmed A, Rich MW, Fleg JL, et al. Effects of digoxin on morbidity and mortality in diastolic heart failure: he ancillary digitalis investigation group trial. Circulation 2006;114:397–403.

8. Cleland JGF, Tendera M, Adamus J, Freemantle N, Polonski L, Taylor J. The Perindopril in Elderly People with Chronic Heart Failure (PEP-CHF) study. Eur Heart J 2006;27:2338–45.

9. Massie BM, Carson PE, McMurray JJ, et al. Irbesartan in patients with heart failure and preserved ejection fraction. N Engl J Med 2008: 2456–67.

10. van Veldhuisen DJ, Cohen-Solal A, Böhm M, et al. Beta-blockade with nebivolol in elderly heart failure patients with impaired and preserved left ventricular ejection fraction. Data from SENIORS (Study of Effects of Nebivolol Intervention on Outcomes and Rehospitalization in Seniors With Heart Failure). J Am Coll Cardiol 2009;53:2150–8.

11. Persson H, Lonn E, Edner M, et al. Diastolic dysfunction in heart failure with preserved systolic function: need for objective evidence. results from the CHARM Echocardiographic Substudy-CHARMES. J Am Coll Cardiol 2007;49:687–94.

12. Louridas G, Lourida K. Heart failure in patients with preserved ejection fraction: questions concerning clinical progression. J Cardiovasc Dev Dis 2016;3:27.

13. Vaduganathan M, Patel RB, Michel A, et al. Mode of death in heart failure with preserved ejection fraction. J Am Coll Cardiol 2017;69: 556–69.

14. Valero-Muñoz M, Backman W, Sam F. Murine models of heart failure with preserved ejection fraction: a "fishing expedition." J Am Coll Cardiol Basic Transl Sci 2017;2:770–89.

15. Roh J, Houstis N, Rosenzweig A. Why don't we have proven treatments for HFpEF? Circ Res 2017; 120:1243–5.

16. Krum H, Teerlink JR. Medical therapy for chronic heart failure. Lancet 2011;378:713–21.

17. Morrissey RP, Czer L, Shah PK. Chronic heart failure: current evidence, challenges to therapy, and future directions. Am J Cardiovasc Drugs 2011; 11:153–71.

18. Bui Anh L, Horwish, Tamara B, Fonarow, Gregg C. Epidemiology and risk profile of heart failure. Nat Publ Gr 2012;8:1–25.

19. Lam CSP, Donal E, Kraigher-Krainer E, Vasan RS. Epidemiology and clinical course of heart failure with preserved ejection fraction. Eur J Heart Fail 2011;13:18–28.

20. Zile MR, Brutsaert DL. New concepts in diastolic dysfunction and diastolic heart failure: part I: diagnosis, prognosis, and measurements of diastolic function. Circulation 2002;105:1387–93.

21. Zile MR, Brutsaert DL. New concepts in diastolic dysfunction and diastolic heart failure: part II. Causal mechanisms and treatment. Circulation 2002;105:1503–8.

22. Yarbrough WM, Mukherjee R, Stroud RE, et al. Progressive induction of left ventricular pressure overload in a large animal model elicits myocardial remodeling and a unique matrix signature. J Thorac Cardiovasc Surg 2012;143:215–23.

23. Romito E, Shazly T, Spinale FG. In vivo assessment of regional mechanics post-myocardial infarction: a focus on the road ahead. J Appl Physiol 2017;123:728–45.

24. Ibrahim E-SH. Myocardial tagging by cardiovascular magnetic resonance: evolution of techniques-pulse sequences, analysis algorithms, and applications. J Cardiovasc Magn Reson 2011;13:36.

25. Strotmann JM, Hatle L, Sutherland GR. Doppler myocardial imaging in the assessment of normal and ischemic myocardial function-past, present and future. Int J Cardiovasc Imaging 2001; 17:89–98.

26. Leitman M, Lysyansky P, Sidenko S, et al. Two-dimensional strain - a novel software for real-time quantitative echocardiographic assessment of myocardial function. J Am Soc Echocardiogr 2004; 17:1021–9.

27. Argulian E, Chandrashekhar Y, Shah SJ, et al. Teasing apart heart failure with preserved ejection fraction phenotypes with echocardiographic imaging: potential approach to research and clinical practice. Circ Res 2018;122:23–5.

28. Kraigher-Krainer E, Shah AM, Gupta DK, et al. Impaired systolic function by strain imaging in heart failure with preserved ejection fraction. J Am Coll Cardiol 2014;63:447–56.

29. Shah AM, Claggett B, Sweitzer NK, et al. Prognostic importance of impaired systolic function in heart failure with preserved ejection fraction and the impact of spironolactone. Circulation 2015;132:402–14.

30. Kato S, Koide M, Copper IVG, Zile MR. Effects of pressure- or volume-overload hypertrophy on passive stiffness in isolated adult cardiac muscle cells. Am J Physiol Heart Circ Physiol 1996;271: 2575–83.

31. Jalil JE, Doering CW, Janicki JS, Pick R, Shroff SG, Weber KT. Fibrillar collagen and myocardial stiffness in the intact hypertrophied rat left ventricle. Circ Res 1989;64:1041–50.

32. Grossman W, Mclaurin LP, Stefadouros MA. Left ventricular stiffness associated with chronic pressure and volume overloads in man. Circ Res 1974;35:793–800.

33. Miyoshi H, Oishi Y, Mizuguchi Y, et al. Effect of an increase in left ventricular pressure overload on left atrial-left ventricular coupling in patients with hypertension: a two-dimensional speckle tracking echocardiographic study. Echocardiography 2013; 30:658–66.

34. Schnelle M, Catibog N, Zhang M, et al. Echocardiographic evaluation of diastolic function in mouse models of heart disease. J Mol Cell Cardiol 2018;114:20–8.

35. Zile MR, Adamson PB, Cho YK, et al. Hemodynamic factors associated with acute decompensated heart failure: part 2-use in automated detection. J Card Fail 2011;17:282–91.

36. Zhao L, Cheng G, Jin R, et al. Deletion of interleukin-6 attenuates pressure overload-induced left ventricular hypertrophy and dysfunction. Circ Res 2016;118:1918–29.

37. Epstein AM, Jha AK, Orav EJ. The relationship between hospital admission rates and rehospitalizations. N Engl J Med 2011;365:2287–95.

38. Barlow SC, Doviak H, Jacobs J, et al. Intracoronary delivery of recombinant TIMP-3 after myocardial infarction: effects on myocardial remodeling and function. Am J Physiol Hear Circ Physiol 2017;313:H690–9.

39. Torres WM, Jacobs J, Doviak H, et al. Regional and temporal changes in left ventricular strain and stiffness in a porcine model of myocardial infarction. Am J Physiol Circ Physiol 2018:958–67.

40. Devereux RB, Alonso DR, Lutas EM, et al. Echocardiographic assessment of left ventricular hypertrophy: comparison to necropsy findings. Am J Cardiol 1986;57:450–8.

41. Biering-Sørensen T, Mogelvang R, Schnohr P, Jensen JS. Cardiac time intervals measured by tissue Doppler imaging M-mode: association with hypertension, left ventricular geometry, and future ischemic cardiovascular diseases. J Am Heart Assoc 2016;5:1–14.

42. Janz RF. Estimation of local myocardial stress. Am J Physiol 1982;242:H875–81.

43. Batson G, Chandrasekhar K, Payas Y, Rickards D. Comparison of pulmonary wedge pressure measured by the flow directed Swan-Ganz catheter with left atrial pressure. Br Heart J 1971;33:616.

44. Zile MR, Tanaka R, Lindroth JR, Spinale F, Carabello BA, Mirsky I. Left ventricular volume determined echocardiographically by assuming a constant left ventricular epicardial long-axis/short-axis dimension ratio throughout the cardiac cycle. J Am Coll Cardiol 1992;20:986–93.

45. Mirsky I, Pasipoularides A. Clinical assessment of diastolic function. Prog Cardiovasc Dis 1990;4: 291–318.

46. Tomita M, Spinale F, Crawford FA, Zile MR. Changes in left ventricular volume , mass, and function during the development and regression of supraventricular tachycardia-induced cardiomyopathy. Circulation 1991;83:635–45.

47. Zile MR, Baicu CF, Gaasch WH. Diastolic heart failure — abnormalities in active relaxation and passive stiffness of the left ventricle. N Engl J Med 2004;350:1953–9.

48. Braunwald E. Heart Disease: A Textbook of Cardiovascular Disease. 5th ed. Philadelphia: WB Saunders, 1997.

49. Baicu CF, Zile MR, Aurigemma GP, Gaasch WH. Left ventricular systolic performance, function, and contractility in patients with diastolic heart failure. Circulation 2005;111:2306–12.

50. Stalling D, Westerhoff M, Hege H. Amira: a highly interactive system for visual data analysis. Vis Handb 2005;1:749–67.

51. Rigort A, Günther D, Hegerl R, et al. Automated segmentation of electron tomograms for a quantitative description of actin filament networks. J Struct Biol 2012;177:135–44.

52. Weber B, Greenan G, Prohaska S, et al. Automated tracing of microtubules in electron tomograms of plastic embedded samples of Caenorhabditis elegans embryos. J Struct Biol 2012;178:129–38.

53. Blom AS, Mukherjee R, Pilla JJ, et al. Cardiac support device modifies left ventricular geometry and myocardial structure after myocardial infarction. Circulation 2005;112:1274–83.

54. Purcell BP, Barlow SC, Perreault PE, et al. Delivery of a matrix metalloproteinase-responsive hydrogel releasing TIMP-3 after myocardial infarction: effects on left ventricular remodeling. Am J Physiol Hear Circ Physiol 2018;315:H814–25.

55. Asahi M, Nakayama H, Tada M, Otsu K. Regulation of sarco(endo)plasmic reticulum Ca2+ adenosine triphosphatase by phospholamban and sarcolipin: implication for cardiac hypertrophy and failure. Trends Cardiovasc Med 2003;13:152–7.

56. Zhihao L, Jingyu N, Lan L, et al. SERCA2a: a key protein in the Ca2+ cycle of the heart failure. Heart Fail Rev 2019 Nov 7 [E-pub ahead of print].

57. Van Essen GJ, Hekkert MTL, Sorop O, et al. Cardiovascular function of modern pigs does not comply with allometric scaling laws. Sci Rep 2018; 8:1–10.

58. Tharp CA, Haywood ME, Sbaizero O, Taylor MRG, Mestroni L. The giant protein titin's role in cardiomyopathy: genetic, transcriptional, and post-translational modifications of TTN and their contribution to cardiac disease. Front Physiol 2019;10:1–8.

59. Zile MR, Baicu CF, Gaasch WH. Diastolic heart failure-abnormalities in active relaxation and passive stiffness of the left ventricle. N Engl J Med 2004;350:1953–9.

60. Bakdash JZ, Marusich LR. Repeated measures correlation. Front Psychol 2017;8:1–13.

61. Kitzman DW, Rich MW. Age disparities in heart failure research. JAMA 2010;304:1950–1.

62. Marwick TH, Shah SJ, Thomas JD. Myocardial strain in the assessment of patients with heart failure: a review. JAMA Cardiol 2019;4:287–94.

63. Phelan D, Collier P, Thavendiranathan P, et al. Relative apical sparing of longitudinal strain using two-dimensional speckle-tracking echocardiography is both sensitive and specific for the diagnosis of cardiac amyloidosis. Heart 2012;98:1442–8.

64. Castano A, Narotsky DL, Hamid N, et al. Unveiling transthyretin cardiac amyloidosis and its predictors among elderly patients with severe aortic stenosis undergoing transcatheter aortic valve replacement. Eur Heart J 2017;38:2879–87.

65. Liu D, Hu K, Niemann M, et al. Effect of combined systolic and diastolic functional parameter assessment for differentiation of cardiac amyloidosis from other causes of concentric left ventricular hypertrophy. Circ Cardiovasc Imaging 2013;6:1066–72.

66. Phan TT, Shivu GN, Abozguia K, Gnanadevan M, Ahmed I, Frenneaux M. Left ventricular torsion and strain patterns in heart failure with normal ejection fraction are similar to age-

related changes. Eur J Echocardiogr 2009;10:793–800.

67. Grossman W, Jones D, McLaurin LP. Wall stress and patterns of hypertrophy in the human left ventricle. J Clin Invest 1975;56:56–64.

68. Mirsky I, Laks MM. Time course of changes in the mechanical-properties of the canine right and left-ventricles during hypertrophy caused by pressure overload. Circ Res 1980;46:530–42.

69. Stroud JD, Baicu CF, Barnes MA, et al. Viscoelastic properties of pressure overload hypertrophied myocardium: effect of serine protease treatment. Am J Physiol Heart Circ Physiol 2013;5799:2324–35.

70. Yin FC, Spurgeon H a, Weisfeldt ML, Lakatta EG. Mechanical properties of myocardium from hypertrophied rat hearts. A comparison between hypertrophy induced by senescence and by aortic banding. Circ Res 1980;46:292–300.

71. Freedman BR, Bade ND, Riggin CN, et al. The (dys)functional extracellular matrix. Biochim Biophys Acta Mol Cell Res 2015;1853:3153–64.

72. Park DW, Sebastiani A, Yap CH, Simon MA, Kim K. Quantification of coupled stiffness and fiber orientation remodeling in hypertensive rat right-ventricular myocardium using 3D ultrasound speckle tracking with biaxial testing. PLoS One 2016;11:1–16.

73. Spinale FG, Janicki JS, Zile MR. Membrane-associated matrix proteolysis and heart failure. Circ Res 2013;112:195–208.

74. Azevedo CF, Nigri M, Higuchi ML, et al. Prognostic significance of myocardial fibrosis quantification by histopathology and magnetic resonance imaging in patients with severe aortic valve disease. J Am Coll Cardiol 2010;56:278–87.

75. Schubert A, Binner C. Extracellular matrix gene expression correlates to left ventricular mass index after surgical induction of left ventricular hypertrophy. Basic Cardiol Res 2001;387:381–7.

76. Spinale FG. Matrix metalloproteinases: regulation and dysregulation in the failing heart. Circ Res 2002;90:520–30.

77. Goldsmith EC, Bradshaw AD, Spinale FG. Cellular mechanisms of tissue fibrosis. 2. Contributory pathways leading to myocardial fibrosis: moving beyond collagen expression. Am J Physiol Cell Physiol 2013;304:C393–402.

78. Monrad ES, Hess OM, Nonogi H, Corin WJ, Krayenbuehl HP. Time course of regression of left ventricular hypertrophy after aortic valve replacement. Circulation 1988;77:1345–55.

79. Villari B, Vassalli G, Monrad ES, Chiariello M, Turina M, Hess OM. Normalization of diastolic dysfunction in aortic stenosis late after valve replacement. Circulation 1995;91:2353–8.

80. Krayenbuehl HP, Hess OM, Monrad ES, Schneider J, Mall G, Turina M. Left ventricular myocardial structure in aortic valve disease before, intermediate, and late after aortic valve replacement. Circulation 1989;79:744–55.

81. Hess OM, Ritter M, Schneider J, Grimm J, Turina M, Krayenbuehl HP. Diastolic stifness and myocardial structure in aortic valve disease before and after valve replacement. Circulation 1984;69:855–65.

82. Roach MR, Burton AC. The reason for the shape of the distensibility curves of arteries. Can J Biochem Physiol 1957;35:681–90.

83. Granzier HL, Labeit S. The giant protein titin: a major player in myocardial mechanics, signaling, and disease. Circ Res 2004;94:284–95.

84. Holmes JW, Borg TK, Covell JW. Structure and mechanics of healing myocardial infarcts. Annu Rev Biomed Eng 2005;7:223–53.

85. Taber LA, Humphrey JD. Stress-modulated growth, residual stress, and vascular heterogeneity. J Biomech Eng 2001;123:528–35.

86. Ambrosi D, Ateshian GA, Arruda EM, et al. Perspectives on biological growth and remodeling. J Mech Phys Solids 2011;59:863–83.

87. Hariton I, DeBotton G, Gasser TC, Holzapfel GA. Stress-driven collagen fiber remodeling in arterial walls. Biomech Model Mechanobiol 2007;6:163–75.

88. Taber LA. Biomechanics of growth, remodeling, and morphogenesis. Appl Mech Rev 1995;48:487–545.

89. Fung YC. Stress, strain, growth, and remodeling of living organisms. Z Angew Math Phys 1995;46:S469–82.

90. Savarese G, Orsini N, Hage C, et al. Utilizing NT-proBNP for Eligibility and Enrichment in Trials in HFpEF, HFmrEF, and HFrEF. J Am Coll Cardiol HF 2018;6:246–56.

91. Koide M, Hamawaki M, Narishige T, et al. Microtubule depolymerization normalizes in vivo myocardial contractile function in dogs with pressure-overload left ventricular hypertrophy. Circulation 2000;102:1045–52.

KEY WORDS heart failure, echocardiography, pressure overload